SCIENCE AND TECHNOLOGY OF ADVANCED MATERIALS
2024, VOL. 25, NO. 1, 2421746
https://doi.org/10.1080/14686996.2024.2421746

Taylor & Francis
Taylor & Francis Group

FOCUS ISSUE ARTICLE

OPEN ACCESS Check for updates

Metastable body-centered cubic CoMnFe alloy films with perpendicular magnetic anisotropy for spintronics memory

Deepak Kumar[a*], Mio Ishibashi[a*], Tufan Roy[b], Masahito Tsujikawa[c], Masafumi Shirai[c,b] and Shigemi Mizukami[a,b]

[a]WPI Advanced Institute for Materials Research, Tohoku University, Sendai, Japan;
[b]Center for Science and Innovation in Spintronics, Tohoku University, Sendai, Japan;
[c]Research Institute for Electrical Communication, Tohoku University, Sendai, Japan

ABSTRACT

A body-centered cubic (bcc) FeCo(B) is a current standard magnetic material for perpendicular magnetic tunnel junctions (*p*-MTJs) showing both large tunnel magnetoresistance (TMR) and high interfacial perpendicular magnetic anisotropy (PMA) when MgO is utilized as a barrier material of *p*-MTJs. Since the *p*-MTJ is a key device of current spintronics memory, *i.e.* spin-transfer-torque magnetoresistive random access memory (STT-MRAM), it attracts attention for further advance to explore new magnetic materials showing both large PMA and TMR. However, there have been no such materials other than FeCo(B)/MgO. Here, we report, for the first time, PMA in metastable bcc Co-based alloy, *i.e.* bcc CoMnFe thin films which are known to exhibit large TMR effect when used for electrodes of MTJs with the MgO barrier. The largest intrinsic PMAs were about 0.6 and 0.8 MJ/m^3 in a few nanometer-thick CoMnFe alloy film and multilayer film, respectively. Our *ab-initio* calculation suggested that PMA originates from tetragonal strain and the value exceeds 1 MJ/m^3 with optimizing strain and alloys composition. The simulation of the thermal stability factor indicates that the magnetic properties obtained satisfy the requirement of the data retention performance of *X*-1*X* nm STT-MRAM. The large PMA and high TMR effect in bcc CoMnFe/MgO, which were rarely observed in materials other than FeCo(B)/MgO, indicate that bcc CoMnFe/MgO is one of the potential candidates of the materials for *X*-1*X* nm STT-MRAM.

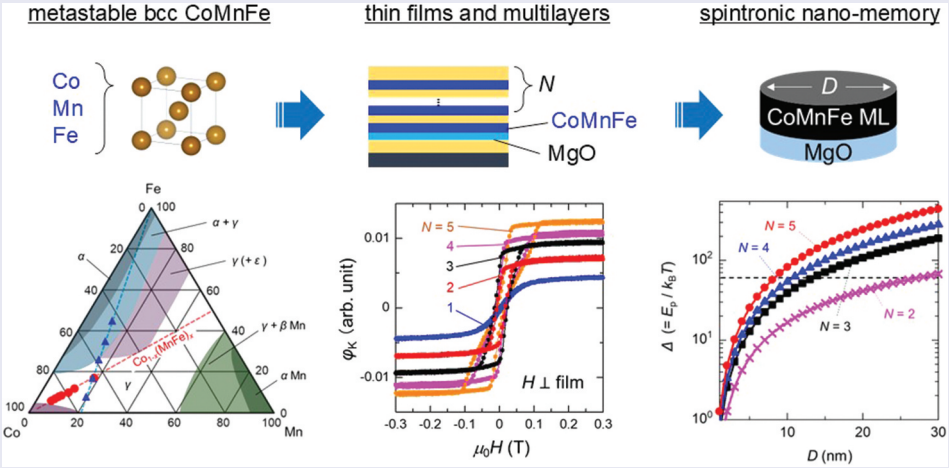

ARTICLE HISTORY
Received 15 September 2024
Revised 20 October 2024
Accepted 22 October 2024

KEYWORDS
perpendicular magnetic anisotropy; metastable alloy; multilayer; thin film; *ab-initio* calculation; MRAM

IMPACT STATEMENT

We discovered large perpendicular magnetic anisotropy, ~0.8 MJ/m^3, in metastable alloys, which are also known to exhibit large tunnel magnetoresistance, demonstrating new candidate for spintronic memory applications.

Introduction

A magnetic tunnel junction (MTJ) consists of an insulating barrier sandwiched by two magnetic electrode layers and exhibits tunnel magnetoresistance (TMR) effect [1,2]. The MTJs utilizing perpendicularly magnetized magnetic electrodes are called perpendicular MTJs (*p*-MTJ), which are applied for spin-transfer-torque magnetoresistive random access memory

CONTACT Shigemi Mizukami shigemi.mizukami.a7@tohoku.ac.jp WPI Advanced Institute for Materials Research, Tohoku University, 2-1-1 Katahira, Aoba-ku, Sendai 980-8577, Japan

*These authors contributed equally to this work.

(STT-MRAM) [3]. The *p*-MTJs also pave the way for future innovations in in-memory computing [4] as well as stochastic computing [5]; thus, the *p*-MTJ is a heart of spintronics applications.

Most of current *p*-MTJs utilize body-centered cubic (bcc) FeCo(B) alloy magnetic electrodes and an MgO barrier [6,7], since large TMR effect was predicted in (001)-oriented Fe/MgO/Fe MTJs in 2001 [8,9] and the concept was proven in Fe(FeCo)/MgO/Fe MTJs in 2004 [10,11]. Large TMR effect is being pursued, to date [12–15]. Such large TMR effect originates from coherent tunnelling of electron in fully spin-polarized energy bands with Δ_1-symmetry along [001] crystallographic direction of Fe and the Δ_1-symmetry filtering effect in MgO(001) [8,9], *i.e.*, a bulk effect. Apart from such bulk effect, an interface of Fe/MgO exhibits another feature, *i.e.*, an interfacial perpendicular magnetic anisotropy (PMA), as first experimentally observed in FeCo(B)/MgO *p*-MTJs in 2010 [7]. The PMA of FeCo(B)/MgO originates from an anisotropic orbital magnetic moment arising from an orbital hybridization of Fe and O atom at the interface [16,17]. These two features, *i.e.*, the large TMR and interfacial PMA, are simultaneously obtained in FeCo(B)/MgO *p*-MTJs and are rarely observed in other systems. Thus, FeCo(B) and MgO are regarded as the standard materials of *p*-MTJs for STT-MRAM.

In STT-MRAM, the magnetization state of *p*-MTJs, parallel or antiparallel of two magnetizations, is regarded as a binary and is maintained via a uniaxial bi-stability thanks to PMA [18]. The magnetization state is read out via the TMR effect and is switched through the current-induced STT in STT-MRAM [18]. Production of embedded type STT-MRAM quite recently started using several-tens-nm laterally-scaled FeCo(B)/MgO *p*-MTJs, and STT-MRAM for *X*-1*X* nm technology nodes are being developed. It is one of the requirements in the current *X*-1*X* nm STT-MRAM technology to find a path to enhance the data retention performance, *i.e.*, the above-mentioned bi-stability in *p*-MTJs, characterized by a thermal stability factor Δ [18]. The Δ is proportional to the effective PMA as well as the magnetic electrode thickness, and $\Delta > 60$ is required for the data retention over 10 years. It has been gradually recognized that the interfacial PMA of FeCo(B)/MgO could not be strong sufficiently for *X*-1*X* nm technology nodes. Therefore, several routes of engineering have been proposed to gain the large Δ, via multi-interfaces of FeCo(B)/MgO [19–23], nano-pilar of FeCo(B)/MgO [24,25], and use of another high PMA materials, such as Pt-doped Co, deposited on FeCo(B) [26]. On the other hand, this issue could also be addressed via an invention of unique magnetic materials exhibiting both TMR large enough and PMA higher than that in FeCo(B)/MgO *p*-MTJs. The finding of such advanced materials is challenging but leads to an innovation in spintronics and STT-MRAM development [27–33].

Here, we focus on bcc Co, which is thermodynamically unstable and is not obtained even as a metastable form [34]. Bcc Co is only available as few monolayer thick films stabilized via an epitaxial strain [35,36]. Although bcc Co may not be suited for practical uses, it is intriguing that bcc Co is theoretically known to show large PMA with tetragonal distortion of bcc crystal structure [37,38]. The physical origin of PMA for bcc Co is different from the interfacial PMA in FeCo(B)/MgO [7,16,17]. In addition, the large TMR effect was also theoretically discussed [39] and was experimentally proven in bcc Co/MgO MTJs [35]. Thus, one route to realize advanced materials showing large TMR and high PMA would be to explore some derivatives from bcc Co obtained as non-equilibrium metastable phase. This concept was partially demonstrated by our recent works on MTJs with about 10-nm-thick electrode films of metastable bcc CoMn and CoMnFe ferromagnetic alloys [40–43]. We have reported, for the first time, the TMR ratio of about 250% at room temperature (RT) in the bcc CoMn/MgO/CoMn MTJs [41]. Moreover, we demonstrated the TMR ratio of about 350% at RT and exceeding 1000% at low temperature in the metastable bcc CoMnFe/MgO/CoMnFe MTJs [Figure 1(a)] [43]. The large TMR effects for CoMnFe/MgO/CoMnFe MTJs were obtained in the MTJs annealed at 350–375°C [43], which almost satisfies the annealing temperature of 400°C required in the back-end-of-line process in STT-MRAM manufacturing [45]. On the other hand, it remained as an issue to elucidate if bcc CoMnFe films show large PMA for *p*-MTJ in STT-MRAM [Figure 1(b)].

In this article, we report, for the first time, PMA in metastable bcc CoMnFe alloy films. Our *ab-initio* calculation suggests that PMA originates from the tetragonal strain and the value of PMA reaches 1 MJ/m^3 with adequate strain and optimized alloy composition. We experimentally confirmed the largest PMA of about 0.6 and 0.8 MJ/m^3 in a few nanometer-thick film and in a multilayer film, respectively. We also observed clear perpendicular magnetization in the multilayer films. The simulation of the thermal stability factor Δ indicates that the magnetic properties obtained satisfy the requirement of the data retention performance of *X*-1*X* nm STT-MRAM. The large PMA and high TMR effect in bcc CoMnFe/MgO, which were rarely observed in materials other than FeCo(B)/MgO, indicate that bcc CoMnFe/MgO is one of the potential candidates of the materials for *X*-1*X* nm STT-MRAM.

Experimental and computational methods

Sample films were fabricated using magnetron sputtering (ULVAC, Inc., Japan) in an ultrahigh vacuum chamber with a base pressure below 2×10^{-7} Pa. The films were deposited at RT onto

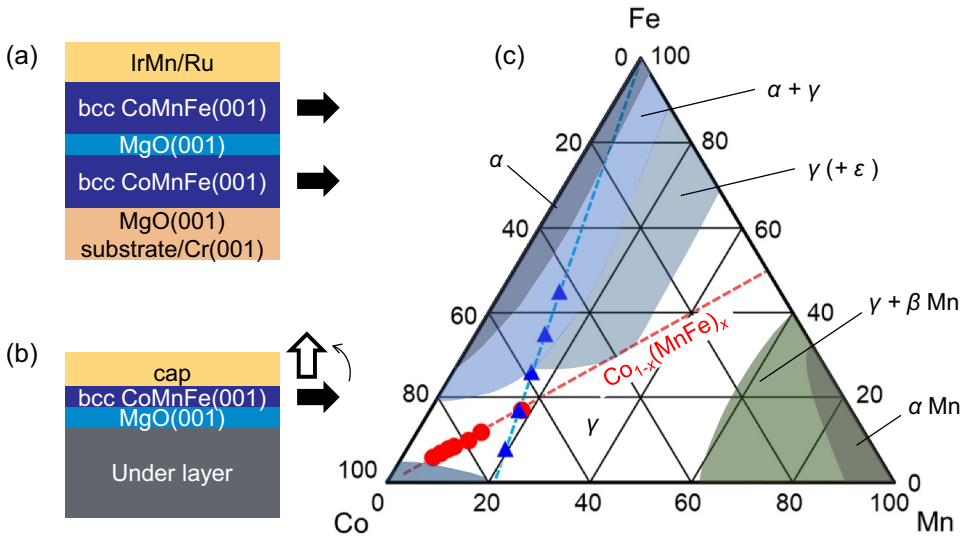

Figure 1. (a) Schematic of an in-plane magnetized magnetic tunnel junction (MTJ) with metastable bcc CoMnFe alloy film electrodes, which were previously studied [43]. (b) Schematic of a metastable bcc CoMnFe alloy film with perpendicular magnetic anisotropy (PMA), which is investigated in the present study. (c) The ternary equilibrium phase diagram of CoMnFe alloys, where α, γ, and ε denote bcc, fcc, and hcp phases, respectively [44]. Solid triangles and circles represent the composition ranges for MTJs previously studied [43] and for films studied here, respectively. Broken lines are visual guides.

substrates of single crystalline MgO(001) via the 40-nm-thick Cr(001) buffer layer. The substrates were heated at 700°C prior to the film depositions and Cr buffer layer was deposited at RT, followed by the post-annealing at 700°C to obtain the atomically flat surface of Cr(001) [40–43]. The composition for the CoMnFe films was varied with co-sputtering technique with a Co elemental and $Co_{60}Mn_{23}Fe_{17}$ alloy targets. Actual film compositions of some samples were analysed with an inductively coupled mass spectrometry (ICP-MS). Magnetic properties were characterized with vibrating sample magnetometer (VSM, Toei Co., Ltd., Japan) and polar magneto-optical Kerr effect (p-MOKE, Neoarc Corp., Japan). The *ab-initio* calculation for magnetic anisotropy is performed with Vienna ab initio simulation package (VASP) [46,47] in combination with projector augmented wave (PAW) method [48]. We used generalized gradient approximation (GGA) for the exchange-correlation energies [49]. The plane-wave cutoff energy was set to 500 eV. We constructed a $2 \times 2 \times 5$ supercell and used special-quasirandom-structures (SQSs) using Alloy-Theoretic Automated Toolkit (ATAT) package to simulate the chemical disorder [50,51]. Brillouin zone integration was performed with $10 \times 10 \times 2$ k-mesh. Finally, magnetic anisotropy energy (MAE) ΔE was obtained from magnetic force theorem [52,53] and was evaluated from the relation: $\Delta E = E_{[100]} - E_{[001]}$, where $E_{[100]}$ and $E_{[001]}$ are the sum of eigen energies for magnetization directions along the crystallographic cubic and/or tetragonal [100] and [001] axes, respectively.

Results and discussions

The TMR effect for in-plane magnetized MTJs with thick metastable bcc CoMnFe electrodes with different compositions

At first, we briefly revisit the TMR effect for the in-plane magnetized MTJs with thick metastable bcc CoMnFe electrodes [43]. We have investigated the TMR effects in the MTJs with $(Co_{0.79}Mn_{0.21})_{1-x}Fe_y$ (y = 0.02–0.45) electrodes with different compositions y, as denoted with the triangles in the ternary phase diagram in Figure 1(c). Stacking structure of those MTJs was MgO(001) substrate/Cr(40)/CoMnFe(10)/MgO(2)/CoMnFe(8)/$Ir_{22}Mn_{78}$(10)/Ru (10) (thickness in nm) [Figure 1(a)], where CoMnFe(001)/MgO(001)/CoMnFe(001) MTJs were epitaxially grown on Cr (001), confirmed via X-ray diffraction measurements [43]. The largest TMR ratios of about 350% at RT and exceeding 1000% at low temperature were observed in the y = 0.08 MTJs, *i.e.*, $Co_{66}Mn_{17}Fe_{17}$, with optimizing the barrier thickness, and so on. At around this composition, the saturation magnetization for bcc CoMnFe was about 1500 kA/m, being slightly larger than the bulk value of Co, about 1400 kA/m, due to the relatively large magnetic moments of Mn and Fe [43,54–57]. Magnetic moments of Mn ferromagnetically couple to those of Co in bcc cells, as unveiled via X-ray magnetic circular dichroism and *ab-initio* calculation studies in the metastable bcc CoMn films [58], which is different from antiferromagnetism in thermodynamically stable fcc/hcp CoMn and fcc CoMnFe alloys [44,59]. Owing to the electronic band structure similar to that of bcc Co [39], the large TMR effect is obtained, *i.e.*, the tunneling mechanism

relevant to the spin-polarized electronic energy bands with Δ_1-symmetry along [001] crystallographic direction of bcc Co, the so-called coherent tunneling [41,43]. It should be noted that the TMR effect of 400% to more than 600% was recently reported in Fe/MgO and FeCo/MgO MTJs [13–15], whereas the TMR effect was smaller in our MTJs with the composition close to FeCo [43]. This difference would be related to some imperfections likely existing in our MTJs at the interface of and/or inside MgO barrier. The TMR ratios in Fe, FeCo, and FeCo(B) MTJs with the MgO barrier variously depend on sample growth methods, preparation conditions, stacking structures, annealing temperatures, and so on [6,7,10–15,35,36,60,61]. There are various discussions on imperfections influencing to the TMR effects, to date [62–67], which may still be open issues to be addressed.

Computational verification of magnetic anisotropy in metastable bcc CoMn alloy

As we mentioned in the introductory part, the strain-induced large magnetic anisotropy of bcc Co was predicted via the *ab-initio* calculation in the past [37]. The strain-induced magnetic anisotropy was also investigated in bcc Fe [37], whereas there is the composition range unexplored for magnetic anisotropy in the ternary phase diagram of bcc CoMnFe alloys, in particular around the composition in which we observed the large TMR effect, as mentioned above. To gain insight into the magnetic anisotropy of metastable bcc CoMnFe alloys, we performed the *ab-initio* calculation of a bulk crystalline MAE ΔE as a function of the composition and tetragonal distortion, as shown in Figure 2(a). Here, for simplicity, we performed the calculation in bcc CoMn binary alloys. In the figure, the positive (negative) sign of ΔE corresponds to a magnetically easy- (hard-) axis parallel to cubic and/or tetragonal [001] direction, *i.e.*, *c* axis. The ΔE is negligible at $c/a \sim 1$ because this MAE arises from the symmetry reduction of cubic crystal structure. In the figure, the sign and magnitude of ΔE *vs.* the axial ratio c/a for pure bcc Co are consistent with those of the previous theoretical calculation [37], where the value for ΔE increases with decreasing the axial ratio c/a. Indeed, our calculation unveiled that the large ΔE is still available even for the CoMn alloys with Co-rich compositions and $c/a < 1$, though the values of ΔE show the opposite trend with decreasing Co concentration in $c/a > 1$.

Experimental verification of PMA of metastable bcc CoMnFe alloy films

Our *ab-initio* calculation of MAE indicates that (001)-oriented bcc CoMnFe films could show PMA when the biaxial in-plane tensile strain is applied and tetragonal distortion is induced in the bcc crystal lattice of the films. Such tensile strain may naturally be applied via an epitaxial growth of very thin films of bcc CoMnFe (001) on top of the MgO(001) barrier, as shown in Figure 2(b), because the lattice constant of bcc CoMnFe is slightly smaller than that of MgO. To verify this concept, we investigated the magnetic properties of very thin films of bcc CoMnFe alloys with different compositions.

We prepared the films of MgO (001) substrate/Cr(40)/Mg(0.4)/MgO(2)/CoMnFe(2)/Cr(3) (thickness in nm), as illustrated in Figure 3(a). The nominal compositions for the films prepared are denoted with solid circles in Figure 1(c). Here, the co-sputtering technique allowed us to obtain the films with the composition approximating to Co_{1-}

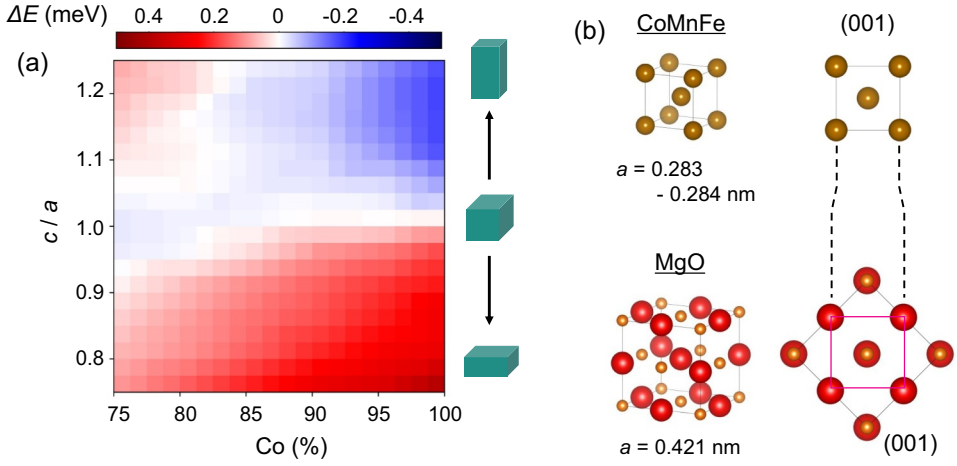

Figure 2. (a) Magnetic anisotropy energy (MAE) ΔE obtained from the *ab-initio* calculation for bcc CoMn alloys as a function of Co composition *x* and axial ratio *c/a*. Positive ΔE corresponds to the magnetically easy axis parallel to *c* ([001]) axis. (b) Schematic of crystal structures of bcc CoMnFe and rocksalt MgO with their lattice constants and the epitaxial relationship of bcc CoMnFe(001) grown on MgO(001).

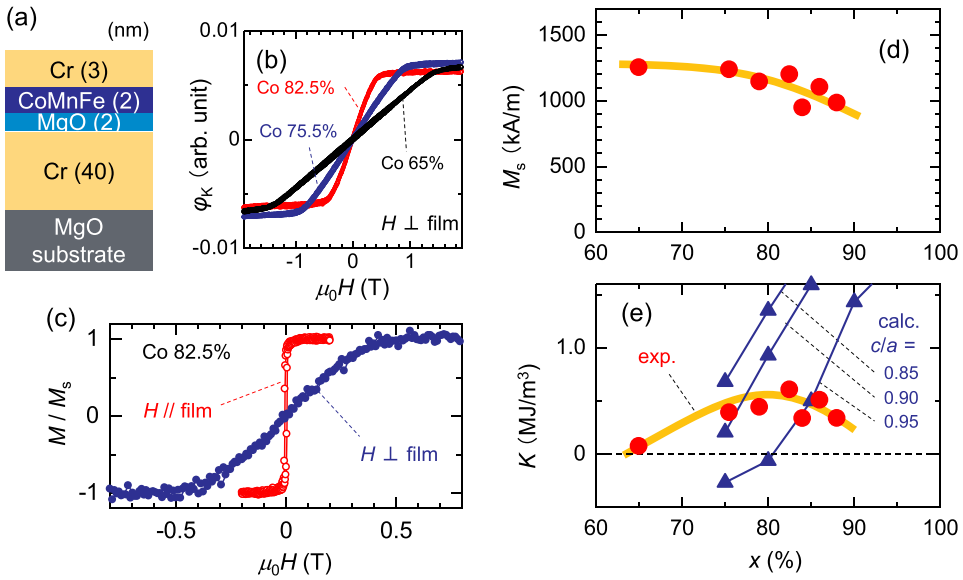

Figure 3. (a) Schematic of a stacking structure of the bcc CoMnFe film studied. (b) Polar magneto-optical Kerr effect (*p*-MOKE) curves for the films with Co concentration of 65, 75.5, and 82.5%. (c) In- and out-of-plane magnetization curves for the film with Co concentration of 82.5%. (d) Saturation magnetization M_s and (e) intrinsic perpendicular magnetic anisotropy (PMA) constant K for the films as a function of the Co concentration x. Solid circles are the experimental values and solid triangles are the values obtained from the *ab-initio* calculation with different values for the axial ratio c/a [Figure 2(a)]. The lines and curves are visual guides.

$_x(\mathrm{MnFe})_x$ ($x < 0.18$), since the actual composition of the alloy film deposited via the $Co_{60}Mn_{23}Fe_{17}$ target was Co:Mn:Fe = 65:18:17 in our sputtering system. Figure 3(b) shows the out-of-plane *p*-MOKE curves for the films with typical compositions. All the films showed in-plane magnetizations at remanent state, whereas those show systematic changes in their out-of-plane saturation magnetic field. This behavior indicates that the sizeable PMA is induced in those films, whereas a shape magnetic anisotropy is still dominant and forces their magnetization being in-plane at remanent state. Figure 3(c) shows the representative magnetization curves, and Figs. 3(d,e) display, respectively, the saturation magnetization M_s and the PMA constant K for the films with different Co compositions. The values of K were obtained via the relation $K = 1/2\ \mu_0 M_s\left(H_{s||}^{\mathrm{eff}} - H_{s\perp}^{\mathrm{eff}}\right) + \mu_0 M_s^2/2$ [68,69]. Here, the effective saturation field H_{sj}^{eff} $(j = ||, \perp)$ was evaluated from the experimental data of the in-plane $(j = ||)$ and out-of-plane $(j = \perp)$ normalized magnetization m_j curve $H_j(m_j)$ via the numerical integration: $H_{sj}^{\mathrm{eff}} = 2\int_0^1 H_j(m_j)dm_j$. For these evaluations, we neglected the contribution of $H_{s||}^{\mathrm{eff}}$ and evaluated the values of $H_{s\perp}^{\mathrm{eff}}$ using the normalized *p*-MOKE curves. The values for M_s were evaluated from the in-plane magnetization measurement for the films. As seen in Figure 3(d), the values for M_s tend to decrease with increasing Co concentration and those values are about 900–1300 kA/m, being smaller than those for 10-nm-thick films, 1400–1500 kA/m. In Figure 3(e), the experimental data of K for the films tend to increase with increasing Co concentration in the range of 65–82.5% and it reaches about 0.6 MJ/m^3 at the Co concentration of 82.5%. The trend of K *vs.* Co concentration in this composition regime is qualitatively consistent with that of the *ab-initio* calculation at $c/a < 1$, as shown in Figure 2(a).

When we assume an ideal pseudomorphic epitaxial growth of bcc CoMnFe(001) on MgO(001), the in-plane lattice constant a of bcc CoMnFe (001) expands up to that of MgO(001), as shown in Figure 2(b), and the out-of-plane lattice constant c of bcc CoMnFe is reduced. With assumption of the conservation of the unit cell volume for bcc CoMnFe with and without the strain, the value of c/a is evaluated as about 0.868 for bcc CoMnFe(001) on MgO(001), where we used the lattice constants of 0.284 [43] and 0.421 nm. Note that the bcc CoMnFe(001) is grown on MgO(001) with an epitaxial relationship of $<100>_{\mathrm{CoMnFe}}$// $<110>_{\mathrm{MgO}}$ [Figure 2(b)]. We also showed the theoretical K values for c/a = 0.85, 0.90, and 0.95 in Figure 3(e). Some experimental values of K are similar to the theoretical K values at c/a of about 0.85–0.90, successfully demonstrating PMA in metastable bcc CoMnFe films, as predicted from the *ab-initio* calculation.

As observed in Figure 3(e), the experimental K values tend to decrease in the films with the Co concentration of more than 82.5%. Although the origin of this reduction of K is not experimentally confirmed at

the present, it is likely that the c/a values tend to be close to unity due to the strain relaxation via introduction of interface misfit dislocations. In other words, the critical thickness, below which the pseudomorphic growth is preserved, becomes smaller than 2 nm at those compositions close to the pure Co. It could also be considered that some structural changes occur due to relatively large lattice mismatch and to reduction of the stability of non-equilibrium bcc phase for the films with the composition close to pure Co.

Observation of perpendicular magnetization and PMA for metastable bcc CoMnFe alloy multilayer films

For further exploring PMA of bcc CoMnFe films, we investigated the effect of multilayered structures on PMA for bcc CoMnFe films. We prepared the films of MgO(001) substrate/Cr(40)/Mg(0.4)/MgO (2)/CoMnFe(1.0)/$[$Cr(0.8)/CoMnFe(1.0)$]_N$/Cr(3) (thickness in nm) with the Co concentration of 82.5% and 86% and different period N for the multilayer, as illustrated in Figure 4(a). Figures 4 (b,c) show the typical out-of-plane p-MOKE curves obtained in the multilayer films with different N for the Co concentration of 82.5% and 86%, respectively. The multilayer films with $N = 1$ show the out-of-plane p-MOKE curves similar to those of the single layer films [Figures 3(b,c)], whereas the hysteresis loops are successfully observed in the multilayer films with $N = 2$–5. The hysteresis loops for the multilayer films with the Co concentration of 82.5% and $N = 3$–5 show the reduction of the remanent value with increasing N. Such hysteresis loop shape would be caused by a nucleation of magnetic domains, as similarly observed in some PMA films [68,70,71].

Figures 5(a,b) show magnetization curves obtained in the multilayer films with $N = 5$ and the Co concentration of 82.5% and 86%, respectively. Figures 5(c,d) display, respectively, the number of CoMnFe layer N +1 dependence of the saturation magnetization M_s and the PMA constant K for the multilayer films. The values of K were obtained with the relation mentioned above with taking account of both $H_{s||}^{eff}$ and $H_{s\perp}^{eff}$ numerically obtained from the normalized magnetization curves measured using VSM. The values for M_s were evaluated from the in-plane magnetization measurement for the multilayer films. As seen in Figures. 5(c,d), the values for M_s and K tend to monotonically increase with increasing N. The value of K reaches about 0.8 MJ/m^3 for the multilayer films with the Co concentration of 82.5% and $N = 5$. The largest value of K in the multilayer films is comparable to the largest value observed in the 2-nm-thick CoMnFe films, as shown in Figure 3(e). In the multilayer films, the strain is induced in the first CoMnFe(001) layer deposited on the MgO(001), then the strain would be sequentially transferred to the next-nearest CoMnFe layers through thin Cr(001) layers in coherently strained multilayer films [68]. Bcc stable thin Cr (001) layers also help to stabilize metastable bcc structure of CoMnFe (001) and mediate magnetic interlayer coupling among the CoMnFe layers. Since the saturation magnetization for the 1-nm-thick CoMnFe is relatively smaller than that for the 2-nm-thick CoMnFe [Figure 5(c)], the intrinsic PMA overcomes the shape magnetic anisotropy, resulting in the perpendicular magnetization in the multilayer films.

Simulation of the thermal stability factor for p-MTJs in STT-MRAM

It is noteworthy that PMA of bcc CoMnFe(001) films on MgO(001) is naturally applicable to the top free type p-MTJs which are currently used in STT-MRAM, where a magnetization of the magnetic layer on the MgO barrier, *i.e.*, a free layer, is switched via the current-induced STT [19–26]. Although various

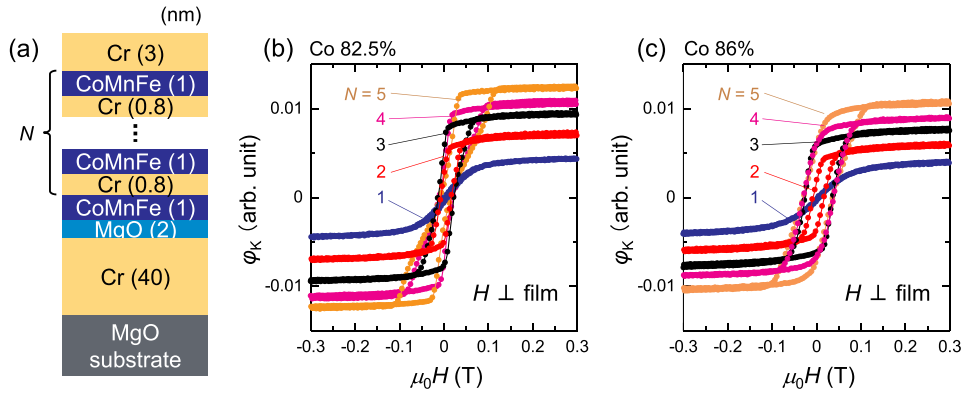

Figure 4. (a) Schematic of a stacking structure of bcc CoMnFe multilayer films. Polar magneto-optical Kerr effect (p-MOKE) curves for the films with Co concentration of 82.5% (b) and 86% (c) with different multilayer period N.

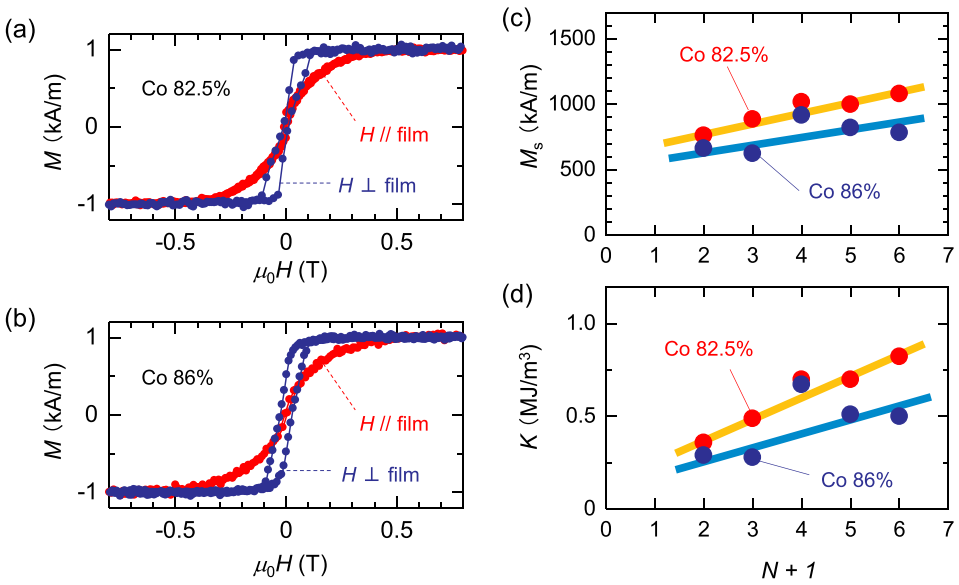

Figure 5. In- and out-of-plane magnetization curves for the multilayer films with Co concentration of (a) 82.5% and (b) 86%. (c) Saturation magnetization M_s and (d) intrinsic perpendicular magnetic anisotropy (PMA) constant K for the multilayer films as a function of the number of CoMnFe layers N +1 with the Co concentration of 82.5% and 86%.

advanced materials are being developed, such as ordered Fe- or Mn-based alloys, most of thin films for those alloys are grown not on MgO(001) but on specific underlayers [29–33]; thus, it could be a future issue to obtain such ordered alloy thin films on the MgO(001) barrier for the top free type *p*-MTJs applications. For further considering the application of bcc CoMnFe films with PMA to the top free type *p*-MTJs in STT-MRAM, we simulated the thermal stability factor Δ, which characterizes the data retention depending on the size of *p*-MTJs in STT-MRAM. We assume the *p*-MTJ with the CoMnFe multilayer as the top free layer having the diameter D and thickness t, as shown in the inset in Figure 6. The calculated values of Δ are shown in Figure 6 as a function of D with different N. In this calculation, we used single domain approximation and the relation $\Delta = E_p/k_BT = K_{eff}V/k_BT$ with $K_{eff} = K - \delta N\mu_0 M_s^2/2$ [24,25,72,73] and the experimentally-obtained values of M_s and K for the multilayer films with the Co concentration of 82.5% and $N = 2$–5 [Figures. 5(c,d)]. Here, E_p is the barrier energy of the bi-stability of the upward and downward direction of the magnetization, $V(=\pi D^2 t/4)$ is the volume of the magnetic layer, k_B is the Boltzmann constant, T is the absolute temperature, and δN is the difference in the dimensionless demagnetization coefficient between the out-of-plane and in-plane orientations [24,25,72,73]. Note that we assume t as a total magnetic layer thickness of the multilayer films. In Figure 6, we observe Δ exceeding 60, which is typically required for the STT-MRAM, for D of about 9 to 15 nm in the case of $N = 3$–5. These results indicate that the magnetic properties, M_s and K, observed in the CoMnFe multilayers with PMA satisfy the requirement for *p*-MTJs used in *X*-1*X* nm STT-MRAM.

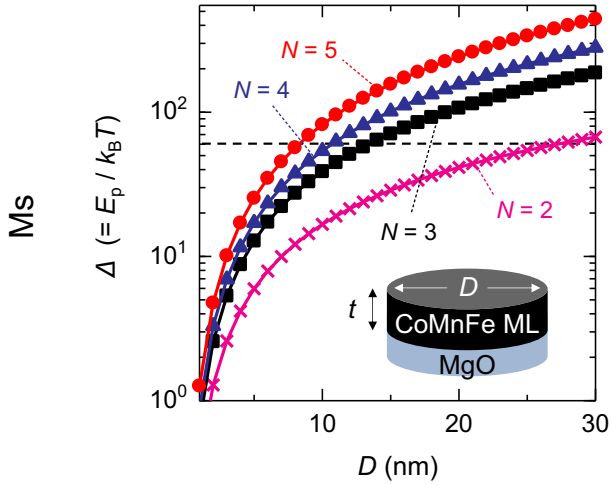

Figure 6. The calculated values of the thermal stability factor Δ at 300 K as a function of the diameter of D for magnetic tunnel junctions (MTJs) with different multilayer period N. Inset shows schematic of the CoMnFe(001) multilayer on MgO (001) barrier for the top free *p*-MTJs with D and thickness t. Broken line shows Δ of 60, a typical requirement for the STT-MRAM applications. The calculation was performed using the magnetic parameters experimentally evaluated in the multilayer films of CoMnFe alloy with Co concentration of 82.5%.

Toward practical STT-MRAM applications

Finally, we briefly discuss low Gilbert damping and manufacturability for the alloy films. Those two properties are also crucial for practical STT-MRAM applications.

As mentioned in the introductory part, the magnetization state is switched through the current-induced STT in STT-MRAM [18]. The threshold of the switching current is proportional to the Gilbert damping constant α [18]. Thus, the low Gilbert damping for magnetic free layer is preferable for low power consumption in STT-MRAM. The Gilbert damping constants of FeCoB/MgO with PMA were variously reported, and typical values are in range from ~0.005 to ~0.03 [7,74–77]. Our past experimental study indicated that the Gilbert damping constants are in range from ~0.004 to ~0.013 for the in-plane magnetized 10-nm-thick bcc $Co_{1-x}Mn_x$ epitaxial films, depending x [78], and this low Gilbert damping was qualitatively consistent with the Gilbert damping constant obtained from the *ab-initio* calculation performed by part of the present authors [78] as well as by the other group [79]. We also preliminary studied the Gilbert damping for the above-mentioned multilayer film with PMA (Co concentration of 82.5% and $N = 5$) using the time-resolved magneto-optical Kerr effect (TRMOKE), and we obtained the effective Gilbert damping constant of ~0.02 (not shown here). This value is in the range for FeCoB/MgO with PMA, as mentioned above. Note that the Gilbert damping constant for very thin films is sensitive to interface properties [76], growth conditions [77], and nonmagnetic layer nearby [80,81], and so on. Such various effects may influence the Gilbert damping constant obtained in our CoMnFe films with PMA.

In STT-MRAM, *p*-MTJs are fabricated on metal lines connecting to semiconductor transistors. For this manufacturing process, (001)-textured polycrystalline FeCoB/MgO *p*-MTJs are utilized in practical STT-MRAM. FeCoB forms (001)-textured polycrystalline film on (001)-textured MgO barrier due to solid phase epitaxy with annealing, which is indeed powerful property and is well suited for the manufacturing [6,82]. Although the present study is performed using epitaxial film samples, (001)-textured polycrystalline films with PMA have to be developed for practical STT-MRAM, like as demonstrated in *p*-MTJs with other candidates of ordered alloys [83]. In principle, bct CoMnFe alloy films with misfit strain may be available even on (001)-textured polycrystalline MgO barrier. This is because crystal orientation relationship of bct CoMnFe(001)<100>|| MgO(001)<110> should maintain in each grain even in (001)-textured polycrystalline films and the misfit strain is generated at those interfaces, as discussed in different context and system [84]. Recently, Yamamoto et al. reported such polycrystalline *p*-MTJs with the top free layer of $Co_{75}Mn_{25}$/Mo/FeCoB with PMA and demonstrated the TMR ratio more than 100% [85]. Since the PMA reported in their *p*-MTJs is still smaller than the values obtained in the present study, further investigation is necessary in poly-crystalline films, as well.

Summary

We recently reported large TMR effect in MTJs with metastable bcc CoMnFe magnetic electrodes [43]. In this study, we explored PMA for this metastable bcc CoMnFe alloy for spintronics applications, in particular STT-MRAM. Our *ab-initio* calculation indicated that the large MAE originates from the tetragonal distortion of bcc crystal lattice and the origin is different from the interface type of PMA in FeCo(B)/MgO. Thin films of bcc CoMnFe layer deposited on the MgO(001) layer exhibited the largest intrinsic PMA of about 0.6 MJ/m^3, as predicted by our *ab-initio* calculation. We also observed the clear perpendicular magnetization in their multilayer films deposited on the MgO(001) layers and obtained the largest intrinsic PMA of about 0.8 MJ/m^3. The simulation of the thermal stability factor Δ suggested that the magnetic properties experimentally obtained in the multilayer films satisfy the data retention requirement for *p*-MJTs in *X*-1*X* nm STT-MRAM. The large PMA and high TMR effect in bcc CoMnFe/MgO, which were rarely observed in materials other than FeCo(B)/MgO, indicate that bcc CoMnFe/MgO is one of the potential candidates of the materials for *X*-1*X* nm STT-MRAM; thus, further studies, including the Gilbert damping and polycrystalline *p*-MTJs, are demanded.

Acknowledgments

We would like to thank Y. Kondo and M. Konno for their technical assistances. S.M. and M.S. thank to Spintronics Research Network in Japan (Spin-RNJ). Figure 2(b) was partly created by VESTA [86]. This research was supported in part by KIOXIA Corporation.

Disclosure statement

No potential conflict of interest was reported by the author(s).

Funding

Core Research for Evolutional Science and Technology [No. JPMJCR17J5]; Ministry of Education, Culture, Sports, Science and Technology, X-NICS [No. JPJ011438].

ORCID

Tufan Roy http://orcid.org/0000-0001-8915-2681
Shigemi Mizukami http://orcid.org/0000-0001-9913-1833

References

[1] Miyazaki T, Tezuka N. Giant magnetic tunneling effect in Fe/Al_2O_3/Fe junction. J Magn Magn Mater. 1995;139(3):L231–L234. doi: 10.1016/0304-8853(95)90001-2

[2] Moodera JS, Kinder LR, Wong TM, et al. Large magnetoresistance at room temperature in ferromagnetic thin film tunnel junction. Phys Rev Lett. 1995;74 (16):3273. doi: 10.1103/PhysRevLett.74.3273
[3] Ikegawa S, Mancoff FB, Janesky J, et al. Magnetoresistive random access memory: present and future. IEEE Trans Electron Dev. 2020;67 (4):1407–1419. doi: 10.1109/TED.2020.2965403
[4] Jung S, Lee H, Myung S, et al. A crossbar array of magnetoresistive memory devices for in-memory computing. Nature. 2022;601(7892):211–216. doi: 10.1038/s41586-021-04196-6
[5] Borders WA, Pervaiz AZ, Fukami S, et al. Integer factorization using stochastic magnetic tunnel junctions. Nature. 2019;573(7774):390–393. doi: 10.1038/s41586-019-1557-9
[6] Djayaprawira DD, Tsunekawa K, Nagai M, et al. 230% room-temperature magnetoresistance in CoFeB/MgO/CoFeB magnetic tunnel junctions. Appl Phys Lett. 2005;86(9):092502. doi: 10.1063/1.1871344
[7] Ikeda S, Miura K, Yamamoto H, et al. A perpendicular-anisotropy CoFeB-MgO magnetic tunnel junction. Nat Mater. 2010;9(9):721–724. doi: 10.1038/nmat2804
[8] Butler WH, Zhang XG, Schulthess TC, et al. Spin-dependent tunneling conductance of Fe|MgO|Fe sandwiches. Phys Rev B. 2001;63(5):054416. doi: 10.1103/PhysRevB.63.054416
[9] Mathon J, Umerski A. Theory of tunneling magnetoresistance of an epitaxial Fe/MgO/Fe(001) junction. Phys Rev B. 2001;63(22):220403. doi: 10.1103/PhysRevB.63.220403
[10] Yuasa S, Nagahama T, Fukushima A, et al. Giant room-temperature magnetoresistance in single-crystal Fe/MgO/Fe magnetic tunnel junctions. Nat Mater. 2004;3(12):868–871. doi: 10.1038/nmat1257
[11] Parkin SSP, Kaiser C, Panchula A, et al. Giant tunneling magnetoresistance at room temperature with MgO (100) tunnel barriers. Nat Mater. 2004;3 (12):862–867. doi: 10.1038/nmat1256
[12] Ikeda S, Hayakawa J, Ashizawa Y, et al. Tunnel magnetoresistance of 604% at 300 K by suppression of Ta diffusion in CoFeB/MgO/CoFeB pseudo-spin-valves annealed at high temperature. Appl Phys Lett. 2008;93(8):082508. doi: 10.1063/1.2976435
[13] Scheike T, Xiang Q, Wen Z, et al. Exceeding 400% tunnel magnetoresistance at room temperature in epitaxial Fe/MgO/Fe(001) spin-valve-type magnetic tunnel junctions. Appl Phys Lett. 2021;118 (4):042411. doi: 10.1063/5.0037972
[14] Scheike T, Wen Z, Sukegawa H, et al. Enhanced tunnel magnetoresistance in Fe/Mg_4Al-O_x/Fe(001) magnetic tunnel junctions. Appl Phys Lett. 2022;120 (3):032404. doi: 10.1063/5.0082715
[15] Scheike T, Wen Z, Sukegawa H, et al. 631% room temperature tunnel magnetoresistance with large oscillation effect in CoFe/MgO/CoFe(001) junctions. Appl Phys Lett. 2023;122(11):112404. doi: 10.1063/5.0145873
[16] Yang HX, Chshiev M, Dieny B, et al. First-principles investigation of the very large perpendicular magnetic anisotropy at Fe|MgO and Co|MgO interfaces. Phys Rev B. 2011;84(5):054401. doi: 10.1103/PhysRevB.84.054401
[17] Dieny B, Chshiev M. Perpendicular magnetic anisotropy at transition metal/oxide interfaces and applications. Rev Mod Phys. 2017;89(2):025008. doi: 10.1103/RevModPhys.89.025008
[18] Yoda H, Kishi T, Nagase T, et al. High efficient spin transfer torque writing on perpendicular magnetic tunnel junctions for high density MRAMs. Cur Appl Phys. 2010;10(1):e87–e89. doi: 10.1016/j.cap.2009.12.021
[19] Sato H, Yamanouchi M, Ikeda S, et al. Perpendicular-anisotropy CoFeB-MgO magnetic tunnel junctions with a MgO/CoFeB/Ta/CoFeB/MgO recording structure. Appl Phys Lett. 2012;101(2):022414. doi: 10.1063/1.4736727
[20] Wang M, Cai W, Cao K, et al. Current-induced magnetization switching in atom-thick tungsten engineered perpendicular magnetic tunnel junctions with large tunnel magnetoresistance. Nat Commun. 2018;9(1):671. doi: 10.1038/s41467-018-03140-z
[21] Nishioka K, Honjo H, Ikeda S, et al. Novel quad-interface MTJ technology and its first demonstration with high thermal stability factor and switching efficiency for STT-MRAM beyond 2X nm. IEEE Trans Electron Dev. 2020;67(3):995–1000. doi: 10.1109/TED.2020.2966731
[22] Honjo H, Nishioka K, Miura S, et al. 25 nm iPMA-type hexa-MTJ with solder reflow capability and endurance > 10^7 for eFlash-type MRAM. In: 2022 International Electron Devices Meeting (IEDM); San Francisco, CA, USA. p. 10.3.1. 10.1109/IEDM45625.2022.10019412.
[23] Igarashi J, Jinnai B, Watanabe K, et al. Single-nanometer CoFeB/MgO magnetic tunnel junctions with high-retention and high-speed capabilities. npj spintronics. 2024;2(1):1. doi: 10.1038/s44306-023-00003-2
[24] Watanabe K, Jinnai B, Fukami S, et al. Shape anisotropy revisited in single-digit nanometer magnetic tunnel junctions. Nat Commun. 2018;9(1):663. doi: 10.1038/s41467-018-03003-7
[25] Perrissin N, Lequeux S, Strelkov N, et al. A highly thermally stable sub-20 nm magnetic random-access memory based on perpendicular shape anisotropy. Nanoscale. 2018;10(25):12187–12195. doi: 10.1039/C8NR01365A
[26] Nakayama M, Oikawa S, Kamata C, et al. 14 nm high-performance MTJ with accelerated STT-Switching and high-retention doped Co-Pt alloy storage layer for 1Z nm MRAM. In: 2023 International Electron Devices Meeting (IEDM); San Francisco, CA, USA; 2023. 1–4. doi: 10.1109/IEDM45741.2023.10413856.
[27] Mizukami S, Sakuma A, Sugihara A, et al. Mn-based hard magnets with small saturation magnetization and low spin relaxation for spintronics. Scr Materialia. 2016;118:70–74. doi: 10.1016/j.scriptamat.2016.01.045
[28] Zhao X, Zhao J. Perpendicularly magnetized Mn_xGa-Based magnetic tunnel junctions: materials, mechanisms, performances, and potential applications. Adv Mater Interface. 2022;9(36):2201606. doi: 10.1002/admi.202201606
[29] Suzuki KZ, Ichinose T, Iihama S, et al. Enhanced tunnel magnetoresistance in Mn-based perpendicular magnetic tunnel junctions utilizing anti-ferromagnetically coupled bcc-Co-based interlayer. Appl Phys Lett. 2021;118(17):172412. doi: 10.1063/5.0042899
[30] Suzuki KZ, Mizukami S. Tunnel magnetoresistance exceeding 100% in magnetic tunnel junctions using Mn-based tetragonal alloy electrodes with

perpendicular magnetic anisotropy. AIP Adv. 2023;13 (3):035225. doi: 10.1063/5.0141706
[31] Garg C, Filippou PC, Ikhtiar, et al. Ferrimagnetic Heusler tunnel junctions with fast spin-transfer torque switching enabled by low magnetization. arXiv:2403.08112. doi: 10.48550/arXiv.2403.08112
[32] Lyu D, Shoup JE, Huang D, et al. Sputtered $L1_0$-FePd and its synthetic antiferromagnet on Si/SiO_2 wafers for scalable spintronics. Adv Funct Mater. 2023;33 (18):2214201. doi: 10.1002/adfm.202214201
[33] Naganuma H, Nishijima M, Adachi H, et al. Unveiling a chemisorbed crystallographically heterogeneous Graphene/L10-FePd interface with a robust and perpendicular orbital moment. ACS Nano. 2022;16(3):4139. doi: 10.1021/acsnano.1c09843
[34] Liu AY, Singh DJ. Elastic instability of bcc cobalt. Phys Rev B. 1993;47(14):8515–8519. doi: 10.1103/PhysRevB.47.8515
[35] Yuasa S, Fukushima A, Kubota H, et al. Giant tunneling magnetoresistance up to 410% at room temperature in fully epitaxial Co/MgO/Co magnetic tunnel junctions with bcc Co(001) electrodes. Appl Phys Lett. 2006;89(4):042505. doi: 10.1063/1.2236268
[36] Andrieu S, Calmels L, Hauet T, et al. Spectroscopic and transport studies of Co_xFe_{1-x}/MgO(001)-based magnetic tunnel junctions. Phys Rev B. 2014;90 (21):214406. doi: 10.1103/PhysRevB.90.214406
[37] Burkert T, Eriksson O, James P, et al. Calculation of uniaxial magnetic anisotropy energy of tetragonal and trigonal Fe, Co, and Ni. Phys Rev B. 2004;69 (10):104426. doi: 10.1103/PhysRevB.69.104426
[38] Vojáček L, Ibrahim F, Hallal A, et al. Giant perpendicular magnetic anisotropy enhancement in MgO-based magnetic tunnel junction by using Co/Fe composite layer. Phys Rev Appl. 2021;15(2):024017. doi: 10.1103/PhysRevApplied.15.024017
[39] Zhang XG, Butler WH. Large magnetoresistance in bcc Co/MgO/Co and FeCo/MgO/FeCo tunnel junctions. Phys Rev B. 2004;70(17):172407. doi: 10.1103/PhysRevB.70.172407
[40] Kunimatsu K, Tsuchiya T, Elphick K, et al. Fabrication of magnetic tunnel junctions with a metastable bcc Co_3Mn disordered alloy as a bottom electrode. Jpn J Appl Phys. 2019;58(8):080908. doi: 10.7567/1347-4065/ab2f96
[41] Kunimatsu K, Tsuchiya T, Roy T, et al. Magnetic tunnel junctions with metastable bcc Co_3Mn electrodes. Appl Phys Express. 2020;13(8):083007. doi: 10.35848/1882-0786/aba883
[42] Elphick K, Yoshida K, Roy T, et al. Lattice softening in metastable bcc Co_xMn_{100-x}(001) ferromagnetic layers for a strain-free magnetic tunnel junction. Phys Rev Appl. 2021;16(5):054052. doi: 10.1103/PhysRevApplied.16.054052
[43] Ichinose T, Ikeda J, Onodera Y, et al. Large tunnel magnetoresistance in magnetic tunnel junctions with magnetic electrodes of metastable body-centered cubic CoMnFe alloys. J Alloys Compd. 2023;960:170750. doi: 10.1016/j.jallcom.2023.170750
[44] Matsui M, Sato K, Adachi K. Magnetic properties of fcc γ-phase in the ternary Co-Mn-Fe system. J Phys Soc Jpn. 1973;35(2):419–425. doi: 10.1143/JPSJ.35.419
[45] Edelstein D, Rizzolo M, Sil D, et al. A 14 nm embedded STT-MRAM CMOS technology. In: 2020 IEEE International Electron Devices Meeting (IEDM); San Francisco, CA, USA. p. 11.5.1–.11.5.4. doi: 10.1109/IEDM13553.2020.9371922.
[46] Kresse G, Furthmüller J. Efficient iterative schemes for *ab initio* total-energy calculations using a plane-wave basis set. Phys Rev B. 1996;54(16):11169–11186. doi: 10.1103/PhysRevB.54.11169
[47] Kresse G, Joubert D. From ultrasoft pseudopotentials to the projector augmented-wave method. Phys Rev B. 1999;59(3):1758–1775. doi: 10.1103/PhysRevB.59.1758
[48] Blöchl PE. Projector augmented-wave method. Phys Rev B. 1994;50(24):17953–17979. doi: 10.1103/PhysRevB.50.17953
[49] Perdew JP, Burke K, Ernzerhof M. Generalized gradient approximation made simple. Phys Rev Lett. 1996;77(18):3865. doi: 10.1103/PhysRevLett.77.3865
[50] Zunger A, Wei SH, Ferreira LG, et al. Special quasirandom structures. Phys Rev Lett. 1990;65(3):353–356. doi: 10.1103/PhysRevLett.65.353
[51] van de Walle A, Tiwary P, De Jong M, et al. Efficient stochastic generation of special quasirandom structures. Calphad. 2013;42:13. doi: 10.1016/j.calphad.2013.06.006
[52] Daalderop GHO, Kelly PJ, Schuurmans MFH. First-principles calculation of the magnetocrystalline anisotropy energy of iron, cobalt, and nickel. Phys Rev B. 1990;41(17):11919–11937. doi: 10.1103/PhysRevB.41.11919
[53] Weinert M, Watson RE, Davenport JW. Total-energy differences and eigenvalue sums. Phys Rev B. 1985;32 (4):2115–2119. doi: 10.1103/PhysRevB.32.2115
[54] Wu D, Liu GL, Jing C, et al. Magnetic structure of $Co_{1-x}Mn_x$ alloys. Phys Rev B. 2001;63(21):214403. doi: 10.1103/PhysRevB.63.214403
[55] Zhang L, Basiaga D, O'Brien JR, et al. Enhanced ferromagnetic phase diagram of epitaxial (Co,Mn) alloys on GaAs(001). J Appl Phys. 2005;98 (10):106101. doi: 10.1063/1.2131187
[56] Snow RJ, Bhatkar H, N'Diaye AT, et al. Enhanced moments in bcc Co1-xMnx on MgO(001). J Magn Magn Mater. 2016;419:490. doi: 10.1016/j.jmmm.2016.06.072
[57] Snow RJ, Bhatkar H, N'Diaye AT, et al. Large moments in bcc $Fe_xCo_yMn_z$ ternary alloy thin films. Appl Phys Lett. 2018;112(7):072403. doi: 10.1063/1.5006347
[58] Kunimatsu K, Roy T, Okabayashi J, et al. Structure and magnetism in metastable bcc $Co_{1-x}Mn_x$ epitaxial films. J Magn Magn Mater. 2022;548:168841. doi: 10.1016/j.jmmm.2021.168841
[59] Ishida K, Nishizawa T. The Co-Mn (cobalt-manganese) system. Bull Alloy Phase Diagrams. 1990;11 (2):25. doi: 10.1007/BF02841695
[60] Wang SG, Ward RCC, Du GX, et al. Temperature dependence of giant tunnel magnetoresistance in epitaxial Fe/MgO/Fe magnetic tunnel junctions. Phys Rev B. 2008;78(18):180411. doi: 10.1103/PhysRevB.78.180411
[61] Bonell F, Hauet T, Andrieu S, et al. Spin-polarized electron tunneling in bcc FeCo/MgO/FeCo(001) magnetic tunnel junctions. Phys Rev Lett. 2012;108 (14):176602. doi: 10.1103/PhysRevLett.108.176602
[62] Klaua M, Ullmann D, Barthel J, et al. Growth, structure, electronic, and magnetic properties of MgO/Fe (001) bilayers and Fe/MgO/Fe(001) trilayers. Phys Rev B. 2001;64(13):134411. doi: 10.1103/PhysRevB.64.134411

[63] Mather PG, Read JC, Buhrman RA. Disorder, defects, and band gaps in ultrathin (001) MgO tunnel barrier layers. Phys Rev B. 2006;73(20):205412. doi: 10.1103/PhysRevB.73.205412
[64] Mathon J, Umerski A. Theory of tunneling magnetoresistance in a disordered Fe/MgO/Fe (001) junction. Phys Rev B. 2006;74(14):140404(R. doi: 10.1103/PhysRevB.74.140404
[65] Ke Y, Xia K, Guo H. Disorder scattering in magnetic tunnel junctions: theory of nonequilibrium vertex correction. Phys Rev Lett. 2008;100(16):166805. doi: 10.1103/PhysRevLett.100.166805
[66] Bonell F, Andrieu S, Tiusan C, et al. Influence of misfit dislocations on the magnetoresistance of MgO-based epitaxial magnetic tunnel junctions. Phys Rev B. 2010;82(9):092405. doi: 10.1103/PhysRevB.82.092405
[67] Taudul B, Monteblanco EN, Halisdemir U, et al. Tunneling spintronics across MgO driven by double oxygen vacancies. Adv Electron Mater. 2017;3(7):1600390. doi: 10.1002/aelm.201600390
[68] Johnson MT, Bloemen PJH, den Broeder FJ, et al. Magnetic anisotropy in metallic multilayers. Rep Prog Phys. 1996;59(11):1409. doi: 10.1088/0034-4885/59/11/002
[69] Gowtham PG, Stiehl GM, Ralph DC, et al. Thickness-dependent magnetoelasticity and its effects on perpendicular magnetic anisotropy in Ta/CoFeB/MgO thin films. Phys Rev B. 2016;93(2):024404. doi: 10.1103/PhysRevB.93.024404
[70] Thiele JU, Folks L, Toney MF, et al. Perpendicular magnetic anisotropy and magnetic domain structure in sputtered epitaxial FePt (001) films. J Appl Phys. 1998;84(10):5686–5692. doi: 10.1063/1.368831
[71] Chesnel K, Westover AS, Richards C, et al. Morphological stripe-bubble transition in remanent magnetic domain patterns of Co/Pt multilayer films and its dependence on Co thickness. Phys Rev B. 2018;98(22):224404. doi: 10.1103/PhysRevB.98.224404
[72] Takeuchi Y, Okuda R, Igarashi J, et al. Nanometer-thin $L1_0$-MnAl film with $B2$-CoAl underlayer for high-speed and high-density STT-MRAM: structure and magnetic properties. Appl Phys Lett. 2022;120(5):052404. doi: 10.1063/5.0077874
[73] Beleggia M, Graef MD, Millev YT. The equivalent ellipsoid of a magnetized body. J Phys D: Appl Phys. 2006;39(5):891. doi: 10.1088/0022-3727/39/5/001
[74] Iihama S, Mizukami S, Naganuma H, et al. Gilbert damping constants of Ta/CoFeB/MgO(Ta) thin films measured by optical detection of precessional magnetization dynamics. Phys Rev B. 2014;89(17):174416. doi: 10.1103/PhysRevB.89.174416
[75] Lattery DM, Zhang D, Zhu J, et al. Low Gilbert Damping Constant in perpendicularly magnetized W/CoFeB/MgO films with high thermal stability. Sci Rep. 2018;8(1):13395. doi: 10.1038/s41598-018-31642-9
[76] Liu E, Lee T, Yang H. Impact of $Fe_{80}B_{20}$ insertion on the properties of dual-MgO perpendicular magnetic tunnel junctions. J Phys D: Appl Phys. 2020;53(45):455004. doi: 10.1088/1361-6463/aba871
[77] Sugihara A, Ichinose T, Tamaru S, et al. Low magnetic damping in an ultrathin CoFeB layer deposited on a 300 mm diameter wafer at cryogenic temperature. Appl Phys Express. 2023;16(2):023003 023003. doi: 10.35848/1882-0786/acbae1
[78] Ogasawara Y, Tsujikawa M, Iihama S, et al. Low Gilbert damping in metastable bcc Co alloys with the addition of Mn, unpublished.
[79] Chimata R, Delczeg-Czirjak EK, Szilva A, et al. Magnetism and ultrafast magnetization dynamics of Co and CoMn alloys at finite temperature. Phys Rev B. 2017;95(21):214417. doi: 10.1103/PhysRevB.95.214417
[80] Mizukami S, Ando Y, Miyazaki T. The study on ferromagnetic resonance linewidth for NM/80NiFe/nm (NM= Cu, Ta, Pd and Pt) films. Jpn J Appl Phys. 2001;40(2R):580–585. doi: 10.1143/JJAP.40.580
[81] Tserkovnyak Y, Brataas A, Bauer GEW. Enhanced Gilbert damping in thin ferromagnetic films. Phys Rev Lett. 2002;88(11):117601. doi: 10.1103/PhysRevLett.88.117601
[82] Yuasa S, Suzuki Y, Katayama T, et al. Characterization of growth and crystallization processes in CoFeB/MgO/CoFeB magnetic tunnel junction structure by reflective high-energy electron diffraction. Appl Phys Lett. 2005;87(24):242503. doi: 10.1063/1.2140612
[83] Gottwald M, Hu G, Trouilloud P, et al. First demonstration of high retention energy barriers and 2 ns switching, using magnetic ordered-alloy-based STT MRAM devices. In: IEEE Symposium on VLSI Technology and Circuits; Honolulu, HI, USA; 2024. p. 1–2. doi: 10.1109/VLSITechnologyandCir46783.2024.10631319.
[84] Wolff N, Jordt P, Jetter J, et al. Nanostabilization of tetragonal distorted FeCo variants in ultra-thin FeCo/TiN multilayer films. Mater Charact. 2021;172:110871. doi: 10.1016/j.matchar.2021.110871
[85] Yamamoto T, Ichinose T, Uzuhashi J, et al. Large tunneling magnetoresistance in perpendicularly magnetized magnetic tunnel junctions using $Co_{75}Mn_{25}$/Mo/$Co_{20}Fe_{60}B_{20}$ multilayers. Phys Rev Appl. 2023;19(2):024020. doi: 10.1103/PhysRevApplied.19.024020
[86] Momma K, Izumi F. VESTA 3 for three-dimensional visualization of crystal, volumetric and morphology data. J Appl Crystallogr. 2011;44(6):1272–1276. doi: 10.1107/S0021889811038970